J. Fluid Mech. (2022), *vol*. 947, A45, doi:10.1017/jfm.2022.667

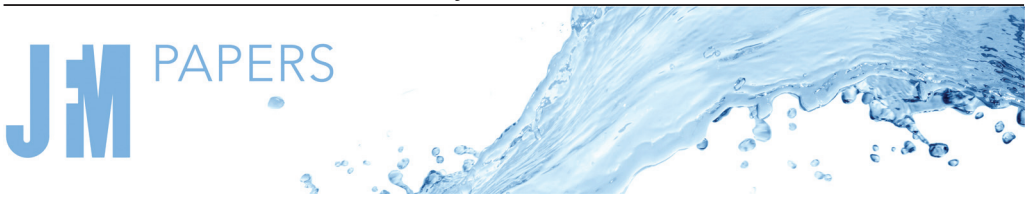

Interaction between an upper-layer point vortex and a bottom topography in a two-layer system

Takaaki Takeuchi[1],† **and Atsushi Kubokawa**[2]

[1]Graduate School of Environmental Science, Hokkaido University, Sapporo, Hokkaido 060-0810, Japan

[2]Faculty of Environmental Earth Science, Hokkaido University, Sapporo, Hokkaido 060-0810, Japan

(Received 16 April 2022; revised 1 July 2022; accepted 27 July 2022)

In this paper, the interaction between an upper-layer vortex and a bottom topography is investigated using an f-plane two-layer quasi-geostrophic model with a point vortex and step-like topography. The contour dynamics method is used to formulate the model. A steadily propagating linear solution along the topography, known as the pseudoimage solution, is derived analytically for a weak point vortex, and the nonlinear solution is obtained numerically. Numerical experiments show that the nonlinear pseudoimage solution collapses with time. Saddle-node points in the velocity field are critical in this collapse. Even after the collapse, the point vortex propagates along the topography similarly to in the steadily propagating solution. Numerical experiments with various initial conditions show that the point vortex has two types of motion in this system: motion along the topography and motion away from the topography. In the latter case, the point vortex and lower-layer potential vorticity anomaly form a heton-like dipole structure. The motion classification results show that an anticyclonic (cyclonic) point vortex on the deeper (shallower) side is more likely to form a dipole structure than a cyclonic (anticyclonic) vortex on the deeper (shallower) side when their initial distance from the topography is the same.

Key words: quasi-geostrophic flows, vortex dynamics, contour dynamics

1. Introduction

Ocean mesoscale eddies play an essential role in water exchange and material circulation. In particular, western boundary regions are well known as areas with western boundary currents characterized by eddy activity, with oceanic eddy termination frequently occurring because the eddies tend to move westward (Chelton, Schlax & Samelson 2011). Since oceanic eddies transport momentum, heat and water masses, investigating

† Email address for correspondence: takeuchi@ees.hokudai.ac.jp

their behaviour is essential for understanding the ocean environment and its variability in the western region (Spall *et al.* 2008; Chelton *et al.* 2011; Baird & Ridgway 2012; Dong *et al.* 2014). Western ocean regions have distinct topography, including continental shelves/slopes. Since distinct topography can play an essential role in the evolution of eddies, the investigation of eddy–topography interactions is critical for understanding the material transport via the movement of eddies (Spall *et al.* 2008; Itoh & Yasuda 2010; Ribbe *et al.* 2018).

A characteristic phenomenon in western boundary regions is that anticyclonic eddies propagate poleward along the coast. On the eastern coast of Japan, Kuroshio warm-core rings have been observed to propagate north (Yasuda, Okuda & Hirai 1992; Kaneko *et al.* 2015). In the South Pacific, many observations have shown that anticyclonic eddies that form off the eastern coast of Australia move poleward along the western boundary (Schaeffer *et al.* 2017; Azis Ismail & Ribbe 2019). Itoh & Sugimoto (2001) numerically reproduced the poleward movement of an eddy that was initially near the topography using primitive equations and found that the effect of the steep bottom slope was an important factor in this motion.

In the open ocean, eddies largely propagate west due to the β-effect; once eddies reach the western boundary, they typically move along that boundary as if they are trapped. However, there is an eastward-propagating solution with a dipole structure. This structure is known as a modon (Stern 1975; Flierl *et al.* 1980). Hughes & Miller (2017) recently observed modons moving eastward in the Tasman Sea using satellite altimeter data and suggested that the bottom topography could play an important role in the formation process. While the modon is a solution consisting of two vortices in the same density layer, a dipole structure with eddies in different layers is also possible. This type of structure is known as a heton (Hogg & Stommel 1985). Since hetons have high heat and material transport capabilities, they are thought to be significant structures in the ocean (Richardson & Tychensky 1998; Morel & McWilliams 2001; Serra & Ambar 2002; Carton *et al.* 2010; Serra, Ambar & Boutov 2010).

Several studies have used idealized models to investigate the interaction between eddies and the bottom topography (Wang 1991; McDonald 1998; Dunn, McDonald & Johnson 2001; White & McDonald 2004; Baker-Yeboah *et al.* 2010; Zhang, Pedlosky & Flierl 2011; de Marez *et al.* 2017). McDonald (1998) and Dunn *et al.* (2001) studied the motion of a point vortex near a step-like topography in a 1.5-layer quasi-geostrophic model in the f-plane. McDonald (1998) found that intense vortices cause a potential vorticity front, which is located along the topography, to wrap around themselves. They defined an intense vortex as one in which the time scale for vortex circulation, T_a, is much shorter than the time scale for topographic wave generation, T_w. Dunn *et al.* (2001) investigated moderate, $T_w \approx T_a$, and weak, $T_w \ll T_a$, point vortices. They found that a moderate vortex forms a dipole structure consisting of a point vortex and the vortex caused by potential vorticity conservation, while a weak vortex propagates steadily along the topography. They analytically showed that a weak vortex propagates parallel to the topography. They referred to this phenomenon as the pseudoimage of the vortex and derived its linear solution. Other studies have also confirmed that the interaction of a vortex with a step-like topography causes propagating vortices along the topography and the formation of dipole structures (Dunn 2002; Dunn, McDonald & Johnson 2002; White & McDonald 2004).

Previous studies focused solely on situations in which vortices were located in the same layer as the topography. However, the interaction between an upper-layer vortex and a lower-layer topography is important to consider for oceanic applications because of density stratification in real environments. Moreover, it is reasonable to hypothesize

that the distance between the topography and the vortex is an important parameter for controlling the system. However, the dependence of this parameter on vortex motion is still unclear. Therefore, we investigated the interaction between the upper vortex and the lower step-like topography using a two-layer quasi-geostrophic model in an f-plane. The purpose of the present study is to clarify the types of motion that occur in this system and the properties of each motion type.

After formulating the problem in § 2, we show the analytical results based on linear theory at the limit of a weak point vortex in § 3. A finite-amplitude pseudoimage solution is derived in § 4. In § 5, we numerically investigate the temporal evolution of both the pseudoimage solution and the system. The conclusions are presented in § 6.

2. Model formulation

2.1. *Potential vorticity and point vortex equations*

In the present study, we used a two-layer quasi-geostrophic model in the f-plane, with the point vortex in the upper layer and the step-like topography in the lower layer (see figure 1). Our model has two layers with an average thickness of H_j and a density of ρ_j, where $j = 1, 2$ denotes the upper and lower layers, respectively. The density in each layer is written in terms of the reference density of the fluid, ρ_0, and the density difference between the two layers, $\Delta\rho$, as $\rho_1 = \rho_0$ and $\rho_2 = \rho_0 + \Delta\rho$. The point vortex in the upper layer has a circulation of Γ and is located at a distance of Y_0 from the topography. In the lower layer, h_B, which denotes the bottom topography, is written as $h_B = -\Delta H \mathrm{sgn}(y)$, where ΔH is the amplitude of the bottom topography and $\mathrm{sgn}(y)$ is the sign function. Assuming that $\Delta H/H_2 \ll 1$, we can use the quasi-geostrophic approximation to formulate this system. The governing equation and the quasi-geostrophic potential vorticity, q_j, in each layer can be written in non-dimensional forms as

$$\frac{\partial q_j}{\partial t} + J(\psi_j, q_j) = 0, \tag{2.1}$$

$$q_1 = \nabla^2\psi_1 - \gamma_L\psi_1 - (\psi_1 - \psi_2), \tag{2.2}$$

$$q_2 = \nabla^2\psi_2 + \gamma_H(\psi_1 - \psi_2) + h_B, \tag{2.3}$$

where t is the time, J is the Jacobian and ψ_j is the streamfunction in the jth layer. The equations in this system were non-dimensionalized using the length scale $L = \sqrt{g'H_1}/f$ and the time scale $T = (f\Delta H/H_2)^{-1}$, where g' is the reduced gravity and f is the Coriolis parameter. We scaled the relative vorticity by $T^{-1} = f\Delta H/H_2$ and the streamfunctions by $L^2T^{-1} = (g'H_1/f)(\Delta H/H_2)$. The non-dimensional amplitude of the point vortex circulation is $\varepsilon = |\Gamma|T/L^2 = |\Gamma|f/(g'H_1)/(\Delta H/H_2)$. The remaining non-dimensional parameters in the equations are $\gamma_H = H_1/H_2$ and $\gamma_L = \Delta\rho/\rho_0$. In addition to these non-dimensional parameters, the initial y-coordinate of the point vortex, Y_0, contributes to the behaviour of this system. Also, Y_0 is non-dimensionalized by L. It should be noted that the streamfunction in the jth layer is invariant under the transformation $\psi_j(x, y) \to -\psi_j(x, -y)$.

Our model has a point vortex in the upper layer and a potential vorticity front that initially lies along the step-like topography, $y = 0$, in the lower layer. Based on the locations of the point vortex, $(X(t), Y(t))$, and the potential vorticity front, $y = \eta(t, x)$,

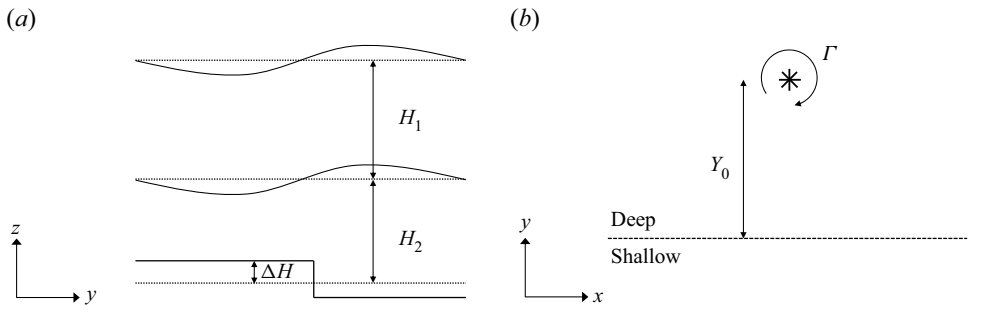

Figure 1. Schematic illustration of the model configuration. (*a*) The cross-section of the two-layer fluid. (*b*) The initial condition for this problem. The point vortex indicated by $*$ is located at $y = Y_0$ and has a circulation of Γ.

we can write the non-dimensional potential vorticity in each layer as

$$q_1 = \varepsilon \mathrm{sgn}(\Gamma)\delta(x - X, y - Y), \tag{2.4}$$

$$q_2 = -\mathrm{sgn}(y - \eta). \tag{2.5}$$

The velocity caused by the topography can be determined based on the potential vorticity anomaly in the lower layer, Δq_2. This anomaly occurs because of the displacement between the potential vorticity front and the topography and is given by

$$\Delta q_2 = \begin{cases} +2, & 0 < y < \eta \\ -2, & \eta < y < 0 \\ 0, & \text{otherwise} \end{cases}. \tag{2.6}$$

In terms of $\eta(t, x)$, $X(t)$ and $Y(t)$, the governing equation in this system can be written as

$$\frac{\partial \eta}{\partial t} + u_2(t, x, \eta)\frac{\partial \eta}{\partial x} = v_2(t, x, \eta), \tag{2.7}$$

$$\frac{\mathrm{d}X}{\mathrm{d}t} = u_1(t, X, Y), \quad \frac{\mathrm{d}Y}{\mathrm{d}t} = v_1(t, X, Y), \tag{2.8}$$

where u_j and v_j are the horizontal components of the velocity and are given by

$$u_j = -\frac{\partial \psi_j}{\partial y}, \quad v_j = \frac{\partial \psi_j}{\partial x}. \tag{2.9a,b}$$

The streamfunction is determined by the equations

$$\nabla^2 \begin{pmatrix} \psi_1 \\ \psi_2 \end{pmatrix} - \boldsymbol{M} \begin{pmatrix} \psi_1 \\ \psi_2 \end{pmatrix} = \begin{pmatrix} \varepsilon \mathrm{sgn}(\Gamma)\delta(x - X, y - Y) \\ \Delta q_2 \end{pmatrix}, \tag{2.10}$$

written in vector form, where the coefficient matrix, $\boldsymbol{M}$, can be written as

$$\boldsymbol{M} = \begin{pmatrix} \gamma_L + 1 & -1 \\ -\gamma_H & \gamma_H \end{pmatrix}. \tag{2.11}$$

2.2. Vertical mode decomposition

The streamfunctions in each layer can be decomposed into vertical modes. The eigenvalues and eigenvectors of $\boldsymbol{M}$ are denoted by $\lambda_\pm$ and $\boldsymbol{V}_\pm = (U_\pm, V_\pm)$, which can be written as

$$\lambda_\pm = \frac{1+\gamma_L+\gamma_H \pm \sqrt{(1+\gamma_L+\gamma_H)^2 - 4\gamma_H\gamma_L}}{2}, \tag{2.12}$$

$$\boldsymbol{V}_\pm = (U_\pm, V_\pm) = \left(1, \frac{1+\gamma_L-\lambda_\pm}{\gamma_H}\right). \tag{2.13}$$

We note that the quantities $\lambda_+^{-1/2}$ and $\lambda_-^{-1/2}$ correspond to the non-dimensional internal and external Rossby radii of deformation, respectively. We can define the streamfunctions of the $+$ and $-$ modes as

$$\psi_\pm = U_\pm\psi_1 + V_\pm\psi_2. \tag{2.14}$$

By substituting (2.14) into (2.10) and using Green's function, we can write $\psi_\pm$ as

$$\psi_\pm(t,x,y) = U_\pm\varepsilon\mathrm{sgn}(\Gamma)G_\pm(x,X,y,Y) + 2V_\pm\int_{-\infty}^{\infty}\mathrm{d}x'\int_0^{\eta(t,x')}\mathrm{d}y'G_\pm(x,x',y,y'), \tag{2.15}$$

where the Green's function in each mode, $G_\pm$, is given by

$$G_\pm(x,x',y,y') = -\frac{1}{2\pi}K_0\left(\sqrt{\lambda_\pm}\sqrt{(x-x')^2+(y-y')^2}\right). \tag{2.16}$$

The streamfunction in each layer, ψ_j, can be obtained from (2.14) and (2.16). We can decompose the streamfunction ψ_j into the point vortex effect, Ψ_j, and the topographic effect, ϕ_j. According to (2.16) and (2.15), the streamfunctions caused by the point vortex can be written as

$$\Psi_1 = \frac{-\varepsilon\mathrm{sgn}(\Gamma)}{V_- - V_+}\left\{V_+G_-(x,X,y,Y) - V_-G_+(x,X,y,Y)\right\}, \tag{2.17}$$

$$\Psi_2 = \frac{\varepsilon\mathrm{sgn}(\Gamma)}{V_- - V_+}\left\{G_-(x,X,y,Y) - G_+(x,X,y,Y)\right\}, \tag{2.18}$$

while those caused by the topography can be written as

$$\phi_1 = \frac{2V_+V_-}{V_- - V_+}\int_{-\infty}^{\infty}\mathrm{d}x'\int_0^{\eta(t,x')}\mathrm{d}y'\left\{G_-(x,x',y,y') - G_+(x,x',y,y')\right\}, \tag{2.19}$$

$$\phi_2 = \frac{2}{V_- - V_+}\int_{-\infty}^{\infty}\mathrm{d}x'\int_0^{\eta(t,x')}\mathrm{d}y'\left\{V_-G_-(x,x',y,y') - V_+G_+(x,x',y,y')\right\}, \tag{2.20}$$

where $U_\pm = 1$.

2.3. Contour dynamics

The flow field in this system is given by (2.9*a*,*b*) and (2.17)–(2.20). The horizontal velocity in the jth layer, $\boldsymbol{u}_j = (u_j, v_j)$, is the sum of the velocity due to the point vortex, $\boldsymbol{u}_j^p$, and the

velocity due to the topography, $\boldsymbol{u}_j^t$. According to (2.17) and (2.18), the velocity in the upper layer due to the point vortex can be written as

$$u_1^p(t,x,y) = \frac{\varepsilon \mathrm{sgn}(\Gamma)}{V_- - V_+}\left\{V_+ \frac{\partial G_-}{\partial y}(x,X,y,Y) - V_- \frac{\partial G_+}{\partial y}(x,X,y,Y)\right\}, \tag{2.21}$$

$$v_1^p(t,x,y) = -\frac{\varepsilon \mathrm{sgn}(\Gamma)}{V_- - V_+}\left\{V_+ \frac{\partial G_-}{\partial x}(x,X,y,Y) - V_- \frac{\partial G_+}{\partial x}(x,X,y,Y)\right\}, \tag{2.22}$$

while the velocity in the lower layer due to the point vortex can be written as

$$u_2^p(t,x,y) = -\frac{\varepsilon \mathrm{sgn}(\Gamma)}{V_- - V_+}\left\{\frac{\partial G_-}{\partial y}(x,X,y,Y) - \frac{\partial G_+}{\partial y}(x,X,y,Y)\right\}, \tag{2.23}$$

$$v_2^p(t,x,y) = \frac{\varepsilon \mathrm{sgn}(\Gamma)}{V_- - V_+}\left\{\frac{\partial G_-}{\partial x}(x,X,y,Y) - \frac{\partial G_+}{\partial x}(x,X,y,Y)\right\}. \tag{2.24}$$

According to (2.19) and (2.20), the velocity in the upper layer due to the topography can be written as

$$u_1^t(t,x,y) = \frac{2V_+V_-}{V_- - V_+}\int_{-\infty}^{\infty} \mathrm{d}x' \left\{G_-(x,x',y,\eta) - G_+(x,x',y,\eta)\right. ,$$
$$\left. -G_-(x,x',y,0) + G_+(x,x',y,0)\right\} \tag{2.25}$$

$$v_1^t(t,x,y) = \frac{2V_+V_-}{V_- - V_+}\int_{-\infty}^{\infty} \mathrm{d}x' \left\{G_-(x,x',y,\eta) - G_+(x,x',y,\eta)\right\}\frac{\partial \eta}{\partial x'}(t,x'), \tag{2.26}$$

while the velocity in the lower layer due to the topography can be written as

$$u_2^t(t,x,y) = \frac{2}{V_- - V_+}\int_{-\infty}^{\infty} \mathrm{d}x' \left\{V_-G_-(x,x',y,\eta) - V_+G_+(x,x',y,\eta)\right. ,$$
$$\left. -V_-G_-(x,x',y,0) + V_+G_+(x,x',y,0)\right\} \tag{2.27}$$

$$v_2^t(t,x,y) = \frac{2}{V_- - V_+}\int_{-\infty}^{\infty} \mathrm{d}x' \left\{V_-G_-(x,x',y,\eta) - V_+G_+(x,x',y,\eta)\right\}\frac{\partial \eta}{\partial x'}(t,x'). \tag{2.28}$$

According to (2.7) and (2.8), we can determine the evolution of the system by using (2.23)–(2.28) to calculate the advection velocity at the front and at the point vortex.

The method of contour dynamics was used in this study to calculate the temporal evolution of the system (Zabusky, Hughes & Roberts 1979). The contour dynamics method allows for an accurate treatment of inviscid fluid dynamics and has been used in numerous studies on the interaction between vortices and potential vorticity fronts (Stern & Flierl 1987; Bell 1989; Wang 1991; McDonald 1998; Dunn *et al.* 2001; Dunn 2002; White & McDonald 2004; Baker-Yeboah *et al.* 2010; Zhang *et al.* 2011).

3. Linear dynamics and pseudoimage solutions

3.1. *Linearized equations*

If we assume that the displacement of the potential vorticity front is small, $|\eta| \ll 1$, and we maintain $|\eta| \ll 1$, we can also assume that $\varepsilon \leq O(|\eta|)$. Then, the governing equation

(2.7) becomes

$$\frac{\partial \eta}{\partial t} = v_2^p(t, x, 0) + v_2^t(t, x, 0), \tag{3.1}$$

where the $O(|\eta|^2)$ terms are neglected. In this approximation, the velocities caused by the topography can be written as

$$u_1^t(t, x, y) = \frac{2V_-V_+}{V_- - V_+} \int_{-\infty}^{\infty} \mathrm{d}x' \left\{ \frac{\partial G_-}{\partial y'}(x, x', y, 0) - \frac{\partial G_+}{\partial y'}(x, x', y, 0) \right\} \eta(t, x'), \tag{3.2}$$

$$v_1^t(t, x, y) = \frac{2V_-V_+}{V_- - V_+} \int_{-\infty}^{\infty} \mathrm{d}x' \left\{ G_-(x, x', y, 0) - G_+(x, x', y, 0) \right\} \frac{\partial \eta}{\partial x'}(t, x'), \tag{3.3}$$

in the upper layer and

$$u_2^t(t, x, y) = \frac{2}{V_- - V_+} \int_{-\infty}^{\infty} \mathrm{d}x' \left\{ V_- \frac{\partial G_-}{\partial y'}(x, x', y, 0) - V_+ \frac{\partial G_+}{\partial y'}(x, x', y, 0) \right\} \eta(t, x'), \tag{3.4}$$

$$v_2^t(t, x, y) = \frac{2}{V_- - V_+} \int_{-\infty}^{\infty} \mathrm{d}x' \left\{ V_- G_-(x, x', y, 0) - V_+ G_+(x, x', y, 0) \right\} \frac{\partial \eta}{\partial x'}(t, x'), \tag{3.5}$$

in the lower layer.

3.2. *Linear topographic wave*

In the absence of a point vortex, we examined the waves governed by linearized equations (3.1). Substituting the form of the wave solution, $\eta = \hat{\eta}_0 \exp\{\mathrm{i}(kx - \omega t)\}$, where $\hat{\eta}_0$ is a constant amplitude, k is the wavenumber in the x-direction and ω is the frequency, into the governing equation, we obtain the condition for the existence of a non-trivial solution, $\hat{\eta}_0 \neq 0$, as

$$\omega = \frac{k}{V_- - V_+} \left(\frac{V_-}{\sqrt{k^2 + \lambda_-}} - \frac{V_+}{\sqrt{k^2 + \lambda_+}} \right), \tag{3.6}$$

where we used both (2.16) and the relation

$$\int_{-\infty}^{\infty} \mathrm{d}x \exp(-\mathrm{i}kx) K_0\left(\sqrt{\lambda_\pm (x^2 + y^2)} \right) = \frac{\pi \exp(-|y|\sqrt{k^2 + \lambda_\pm})}{\sqrt{k^2 + \lambda_\pm}}. \tag{3.7}$$

This relation (3.6) is the dispersion relation for linear topographic Rossby waves propagating along a step-like topography which has been derived by Rhines (1977). According to (3.6), the phase speed and group velocity are

$$c = \frac{1}{V_- - V_+} \left(\frac{V_-}{\sqrt{k^2 + \lambda_-}} - \frac{V_+}{\sqrt{k^2 + \lambda_+}} \right), \tag{3.8}$$

$$c_g = \frac{1}{V_- - V_+} \left(\frac{\lambda_- V_-}{(k^2 + \lambda_-)^{3/2}} - \frac{\lambda_+ V_+}{(k^2 + \lambda_+)^{3/2}} \right), \tag{3.9}$$

respectively. Since $\lambda_- < \lambda_+$ and $V_+ < V_-$ hold for any value of k, c and c_g are always positive.

3.3. *Linear pseudoimage solutions*

In a previous study, Dunn *et al.* (2001) used a 1.5-layer model to show the motion of a point vortex propagating steadily along a step-like topography and referred to this phenomenon as the pseudoimage of the vortex. In this study, we sought to determine the linear solution, referred to as the linear pseudoimage solution, and to investigate the properties of the solution.

To determine the steadily propagating solution of (3.1) that progresses with the point vortex, we assumed that the solution was in the form $\eta = \eta(x - c_{pse}t)$, where the propagating speed, c_{pse}, is given as $c_{pse} \equiv \mathrm{d}X/\mathrm{d}t$. Since $\mathrm{d}X/\mathrm{d}t = u_1^t(t, X, Y) = O(\varepsilon)$, we can consider a situation in which the point vortex is fixed at $(0, Y_0)$. According to (3.1), the governing equation then becomes

$$-c_{pse}\frac{\partial \eta}{\partial x} = \frac{\partial \Psi_2}{\partial x}(x, 0) + \frac{2}{V_- - V_+}\int_{-\infty}^{\infty} \mathrm{d}x' \left\{V_- G_-(x, x', 0, 0) - V_+ G_+(x, x', 0, 0)\right\} \times \frac{\partial \eta}{\partial x'}(t, x'), \tag{3.10}$$

where $v_2^p = \partial \Psi_2/\partial x$. Although the term on the left side in the above equation has an order of $O(\varepsilon^2)$, to investigate the asymmetry of the solution due to the sign of c_{pse}, we leave this term explicitly in the equation. Using both Fourier transform methods and (2.16) and (3.7), we can obtain the solution to (3.10) as

$$\eta(x - c_{pse}) = \frac{1}{2\pi}\int_{-\infty}^{\infty} \mathrm{d}k \frac{\exp(\mathrm{i}k(x - c_{pse}t))}{c - c_{pse}} \mathcal{F}[\Psi_2(x, 0)], \tag{3.11}$$

where c is the phase speed of the topographic Rossby waves (3.8), and $\mathcal{F}[\Psi_2]$ is the Fourier transform of Ψ_2,

$$\mathcal{F}[\Psi_2(x, 0)] = -\frac{1}{2}\frac{\varepsilon \mathrm{sgn}(\Gamma)}{V_- - V_+}\left\{\frac{\exp(-|Y_0|\sqrt{k^2 + \lambda_-})}{\sqrt{k^2 + \lambda_-}} - \frac{\exp(-|Y_0|\sqrt{k^2 + \lambda_+})}{\sqrt{k^2 + \lambda_+}}\right\}. \tag{3.12}$$

By substituting (3.11) into the linearized streamfunction caused by the topography, ϕ_j, we can obtain the linear pseudoimage solution in the two-layer model

$$\phi_1 = \frac{-1}{2\pi}\frac{V_- V_+}{V_- - V_+}\int_{-\infty}^{\infty} \mathrm{d}k \frac{\exp(\mathrm{i}k(x - c_{pse}t))}{c - c_{pse}} \times \left(\frac{\exp(-|y|\sqrt{k^2 + \lambda_-})}{\sqrt{k^2 + \lambda_-}} - \frac{\exp(-|y|\sqrt{k^2 + \lambda_+})}{\sqrt{k^2 + \lambda_+}}\right) \mathcal{F}[\Psi_2(x, 0)], \tag{3.13}$$

$$\phi_2 = \frac{-1}{2\pi}\frac{1}{V_- - V_+}\int_{-\infty}^{\infty} \mathrm{d}k \frac{\exp(\mathrm{i}k(x - c_{pse}t))}{c - c_{pse}} \times \left(\frac{V_- \exp(-|y|\sqrt{k^2 + \lambda_-})}{\sqrt{k^2 + \lambda_-}} - \frac{V_+ \exp(-|y|\sqrt{k^2 + \lambda_+})}{\sqrt{k^2 + \lambda_+}}\right) \mathcal{F}[\Psi_2(x, 0)]. \tag{3.14}$$

The propagating velocity, c_{pse}, is given as

$$c_{pse} = -\frac{\partial \phi_1}{\partial y}(0, Y_0) = \frac{\mathrm{sgn}(Y_0)}{2\pi}\frac{V_- V_+}{V_- - V_+} \times \int_{-\infty}^{\infty} \mathrm{d}k \frac{\exp(-|Y_0|\sqrt{k^2 + \lambda_-}) - \exp(-|Y_0|\sqrt{k^2 + \lambda_+})}{c - c_{pse}} \mathcal{F}[\Psi_2(0, 0)]. \tag{3.15}$$

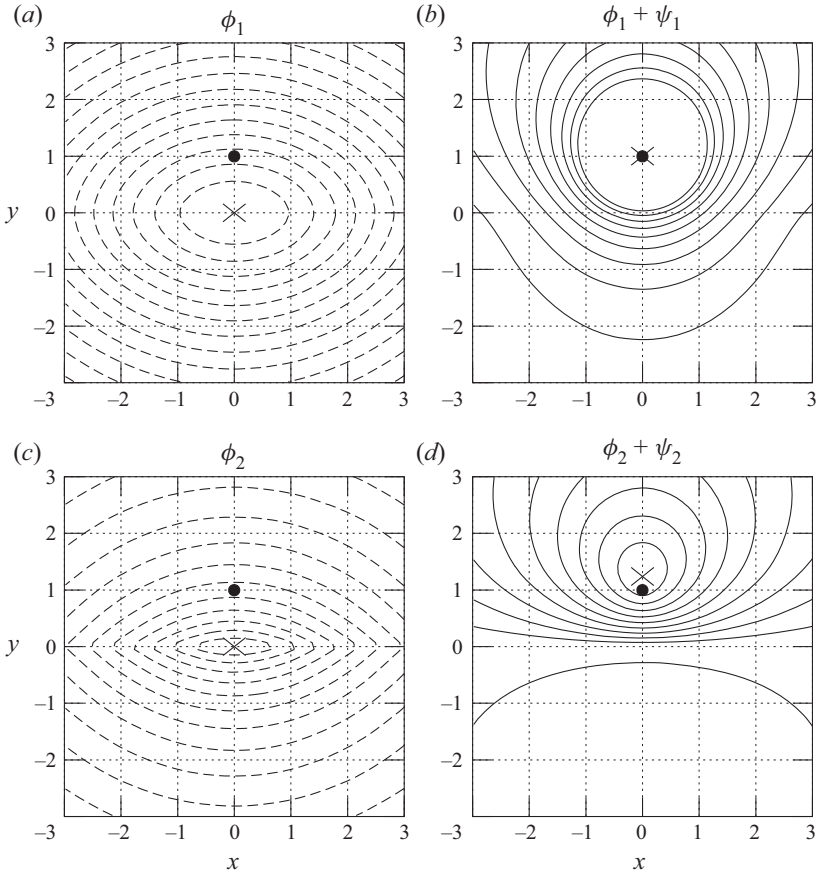

Figure 2. The ϕ_j field (*a*,*c*) and the $\phi_j + \Psi_j$ field (*b*,*d*) of the linear pseudoimage solution in the upper layer (*a*,*b*) and lower layer (*c*,*d*). The positive and negative streamlines are indicated by the solid and dashed lines, respectively. The positions of the maximum or minimum value are denoted by the cross. In the left panels, the contour interval is 0.005, and the minimum values are -0.0235 in the upper layer and -0.0292 in the lower layer. In the right panels, the contour interval is 0.001, and the maximum values are 0.0694 in the upper layer and 0.0098 in the lower layer. In all the cases shown here, $\mathrm{sgn}(\Gamma) = -1$, $\varepsilon = 0.1$, $Y_0 = 1$, $\gamma_L = 10^{-3}$ and $\gamma_H = 1$. The point vortex is indicated by the closed circle at (0,1). The topography is located along $y = 0$.

The sign of c_{pse} is equal to the sign of $Y_0\Gamma$. The fields of the streamfunction, ϕ_j and $\phi_j + \Psi_j$, are shown in figure 2. Although the ϕ_j field is similar to its counterpart in the 1.5-layer model, the $\phi_j + \Psi_j$ field differs from its counterpart. In the 1.5-layer model, the fluid on the opposite side of the point vortex is at rest because the pseudoimage solution completely cancels any effects from the point vortex on this side. In a two-layer model, this cancellation is achieved only in the vicinity of the topography in the lower layer.

3.4. *Small but non-zero amplitude pseudoimage solution*

If we suppose that $0 < \varepsilon \ll 1$ but ε is finite, we can examine the properties of a two-layer pseudoimage with a finite amplitude. In this parameter region, ϕ_j may have poles at the wavenumbers, k_c, that satisfy $c = c_{pse}$. The integrations (3.13) and (3.14) do not include k_c when the point vortex moves in the opposite direction of the topographic waves, i.e. $c_{pse} < 0$. In contrast, if $c_{pse} > 0$, the solutions include a singularity because the path

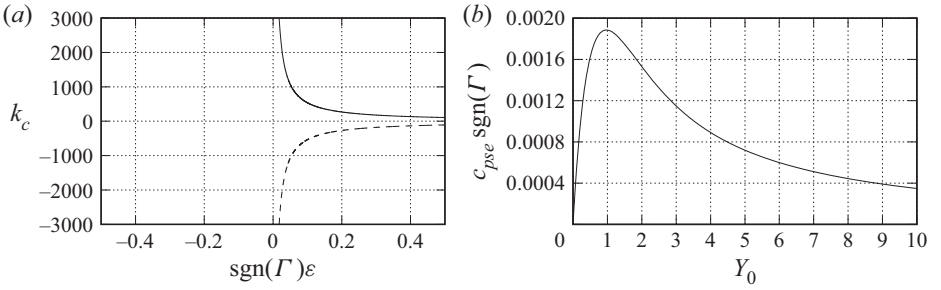

Figure 3. (*a*) The dependencies of the wavenumbers, k_c, which satisfy $c = c_{pse}$ on $\mathrm{sgn}(\Gamma)\varepsilon$ for $Y_0 = 1$ and are calculated from (3.8) and (3.15). Since c is a function of k^2, there are both positive and negative k_c. As $\mathrm{sgn}(\Gamma)\varepsilon \to 0$, $|k_c|$ diverges to infinity. (*b*) The dependence of the propagation velocity, c_{pse}, on Y_0. The propagation velocity has a maximum at approximately $Y_0 = 0.7$. In both panels, $\gamma_H = 1$ and $\gamma_L = 10^{-3}$.

must contain k_c. In the 1.5-layer model, Dunn *et al.* (2001) confirmed that a finite length wave train in the wake of the vortex is excited and that the point vortex drifts towards the topography due to the presence of the singularity. Similar behaviours are expected in the two-layer model. However, since the poles k_c correspond to short waves, the singularity only has a small influence on the pseudoimage solution (see figure 3*a*).

Figure 3(*b*) shows the Y_0 dependence of c_{pse} in the parameter region $0 < \varepsilon \ll 1$. The propagation speed, $|c_{pse}|$, does not monotonically decrease along Y_0, and it has an extreme value at $Y_0 \approx 0.7$. This corresponds to the radial distance in the lower layer where the upper-point vortex has its maximum azimuthal velocity, i.e. the internal Rossby radius of deformation, $\lambda_+^{-1/2} \approx 0.7$. Another feature is that c_{pse} is non-singular as $Y_0 \to 0$. This non-singularity occurs because the lower layer lacks a singular point at the location of the point vortex.

4. Finite-amplitude pseudoimage solution

It is difficult to obtain analytical expressions for finite-amplitude, nonlinear solutions. In this section, we determined finite-amplitude steadily propagating solutions by numerically solving (2.7) with (2.21)–(2.28). According to the linear arguments, the finite-amplitude pseudoimage solutions can exist only when $\mathrm{sgn}(\Gamma Y_0) = -1$. Hence, in this section, we focus on the case of an anticyclonic point vortex at the deeper side.

First, we use the Galilean transformation,

$$x \to \xi = x - c_{pse}t. \tag{4.1}$$

Then, the governing equation can be written as

$$-c_{pse}\frac{\partial \eta}{\partial \xi} + u_2\frac{\partial \eta}{\partial \xi} = v_2. \tag{4.2}$$

As a result, the pseudoimage solutions satisfy the equation

$$\frac{\partial \eta}{\partial \xi} = \frac{v_2}{u_2 - c_{pse}}. \tag{4.3}$$

The boundary condition can be written as

$$\eta \to 0 \quad \text{as } |\xi| \to \infty. \tag{4.4}$$

Furthermore, we assume that the solution is symmetric with $\xi = 0$. Therefore, we have

$$\eta(-\xi) = \eta(\xi). \tag{4.5}$$

We compute η only for $\xi \leq 0$.

To perform the numerical calculations, we discretize the potential vorticity front into N nodes for $-\xi_\infty \leq \xi_n \leq 0$, where $\xi_1 = -\xi_\infty$ and $\xi_N = 0$. Since the contribution of the far field is weak in the integration (2.28) and (2.29), the node spacing near the crest should be fine, whereas the spacing in the far field can be rough. Therefore, we set $\xi_n = \mu_0(n - N)$ for $n \geq N_1$ and $\xi_n = -W + 1 - \mu_0(N_1 - n) - \exp[\mu_0(N_1 - n)/5]$ for $n < N_1$, where $W = \mu_0(N - N_1)$ and $\xi_\infty = W - 1 + \mu_0(N_1 - 1) + \exp[\mu_0(N_1 - 1)/5]$. In this study, we set $\mu_0 = 0.02$, $N = 2650$ and $N_1 = 1150$; thus, we have $W = 30$ and $\xi_\infty \simeq 151$. The finite-difference form of (4.3) is

$$\frac{\eta_{n+1} - \eta_{n-1}}{\xi_{n+1} - \xi_{n-1}} = \frac{v_{2,n}}{u_{2,n} - c_{pse}}, \quad n = 1, \ldots, 2N - 1. \tag{4.6}$$

The boundary conditions at $\xi = \xi_1, \xi_N$ are

$$\eta_1 = 0, \tag{4.7}$$

$$\eta_N = \frac{\eta_{N-1} - \eta_{N-2}}{\xi_{N-1} - \xi_{N-2}}(\xi_N - \xi_{N-1}) + \eta_{N-1}, \tag{4.8}$$

where (4.7) corresponds to (4.4), and (4.8) indicates that the front can be approximated as a quadratic function near the origin. As a result, we can obtain the frontal displacement, η_n, and the propagation velocity, c_{pse}, for the given values of ε by solving (4.6), (4.7), (4.8), with the condition that the solution propagates with the point vortex, $c_{pse} = u_1(0, Y_0)$, where the point vortex is located at $(0, Y_0)$. We used MINPACK (Moreé, Garbow & Hillstrom 1980) to solve the nonlinear simultaneous equations, with the front displacement of the linear solution (3.11) as the initial value in the iterative calculation. In this study, the midpoint method was used for the numerical integration. The validity of the obtained solutions was confirmed by conducting numerical experiments with the solutions as initial conditions. In the following subsections, we set the remaining parameter values as $\gamma_H = 1$, $\gamma_L = 10^{-3}$ and $Y_0 = 1$.

4.1. *Dependency on ε*

Figure 4 shows the frontal displacement and propagation speeds for various values of ε obtained by solving the simultaneous equations. As ε increases, both the displacement and the propagation speed, $|c_{pse}|$, increase. Figure 4(*b*) suggests that the linear solution is valid for small values of ε. Figure 5 shows that the nonlinearity sharpens the peak of the frontal displacement.

4.2. *The saddle-node point*

Figure 6 shows the current vectors caused by the frontal displacement and the point vortex in ξ–y coordinates. There are two saddle-node points in the front with $u_2 - c_{pse} = 0$. Since these points also exist when ε is small, the existence of these points is believed to be a common feature of the pseudoimage solutions. The existence of this point may affect the time evolution of the front as in eddy–jet interactions (Bell & Pratt 1992; Capet & Carton 2004); this will be investigated with numerical experiments in § 5.1.

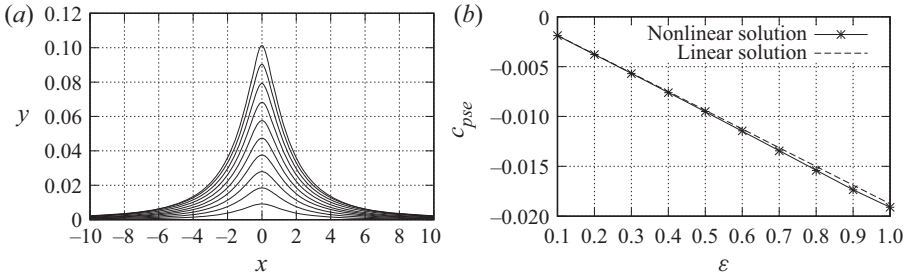

Figure 4. (*a*) The potential vorticity front and (*b*) its propagation speed for each value of ε. Here, ε ranges from 0.1 to 1 in steps of 0.1. The front with the maximum displacement was observed for $\varepsilon = 1$. The propagation speed obtained by the linear solution is indicated by the dashed line in the right panel.

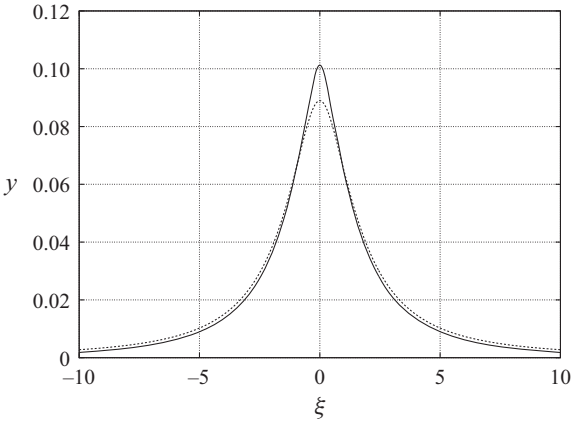

Figure 5. The potential vorticity front of the linear (dashed line) and nonlinear (solid line) solutions for $\varepsilon = 1$.

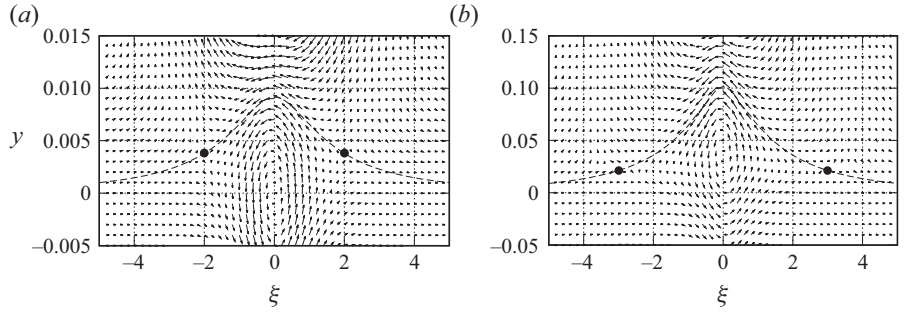

Figure 6. The potential vorticity front of the nonlinear solution and the current vectors caused by the nonlinear solution and the point vortex in ξ–y coordinates. (*a*) Shows the case $\varepsilon = 0.1$, and (*b*) shows the case $\varepsilon = 1$. The closed circles on the front represent the saddle points.

5. Numerical experiments for nonlinear evolution

In this section, we perform numerical experiments. First, we consider the temporal evolution of the pseudoimage solution obtained in the previous section. Then, to investigate the temporal evolution of the system in the parameter space consisting of ε and Y_0, we perform numerical experiments with various initial conditions.

As in the previous section, we resolve the front into discrete nodes with positions (x_n, η_n). From the Lagrangian perspective, the temporal evolution of these nodes can be written as

$$\frac{\mathrm{d}x_n}{\mathrm{d}t} = u_2(t, x_n, \eta_n), \tag{5.1}$$

$$\frac{\mathrm{d}\eta_n}{\mathrm{d}t} = v_2(t, x_n, \eta_n). \tag{5.2}$$

We can determine the temporal evolution of the system by calculating (2.8), (5.1) and (5.2). The velocities advecting the point vortex and the front can be evaluated numerically by calculating (2.21)–(2.28). The numerical integration scheme used to calculate the velocities is the same as in the previous section. The initial node distribution is the same as that in § 4. Since the front near the point vortex elongates with time in its evolution, a new node is added by linear interpolation to keep a spatial resolution when the distance between the adjacent nodes, μ, is $\mu > 1.5\mu_0$, where $\mu_0 = 0.02$. This interpolation is performed in the region of $|x| \leq W$ because the elongation of the front is negligibly small in the region of $|x| > W$, where $W = 30$. When filamentation structures appear, the number of nodes in the front rapidly increases. To avoid calculating a large number of nodes, we use a contour surgery algorithm (Dritschel 1988; Shimada & Kubokawa 1997). In particular, we employ the algorithm described in Shimada & Kubokawa (1997). The validity of the predefined parameter μ_c, the minimum distance between two segments on the front, was verified by comparing the area surrounded by the front and the topography in surgery and no-surgery experiments for several different parameters. The fourth-order Runge–Kutta method was used for time integration in the numerical experiments. The accuracy of the calculation was verified by comparing the phase speed of a small-amplitude sine wave in the absence of a point vortex calculated by the numerical experiment with the analytical result (3.8). All the numerical experiments in this section used $\gamma_L = 10^{-3}$, $\gamma_H = 1$, $\mu_c = 0.002$ and a time step of $\Delta t = 0.01$. The parameters ε and Y_0 are shown for each experiment.

5.1. *Temporal evolution of the pseudoimage*

Figure 7 shows the evolution of the nonlinear pseudoimage solution for $\varepsilon = 1$. Figure 7(*a*) demonstrates that a frontal wave was generated, and that the wavenumber increased as the wave approached the saddle-node point in the direction of movement. Figure 7(*b*) shows that the frontal wave is stationary and grows near the saddle-node points in the coordinate system that moves with the pseudoimage. These features suggest that the symmetry of the pseudoimage solutions is unstable and likely to collapse (see figure 8*a*). On the other hand, the propagation speed of the point vortex remains nearly constant for some time, as shown in figure 8(*b*), suggesting that the interaction between the vortex and the potential vorticity anomaly is insensitive to the shape of the front. The frontal wave dynamics is the same as that of the topographic waves. The phase speed along the front, c_f, can be written as

$$c_f = u_2 + c, \tag{5.3}$$

where u_2 is the velocity along the front and c is given by (3.8). Since the waves are stationary in the moving coordinate system, i.e. $c_f - c_{pse} = 0$, we can calculate the wavenumber as

$$0 = u_2 + c - c_{pse}, \tag{5.4}$$

which shows that k is infinitely large at the stagnation point. Figure 9(*a*) shows the frontal displacement of the frontal wave at $t = 50$, which we can use to estimate the local

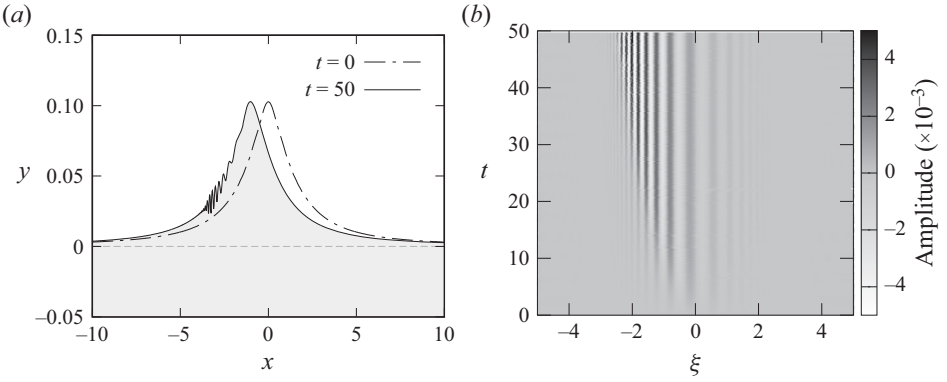

Figure 7. (*a*) Temporal evolution of the front of the nonlinear solution for $\varepsilon = 1$. The solid line corresponds to the front at $t = 50$, while the dash-dotted line corresponds to the front at $t = 0$. The fluid in the shaded area has a higher potential vorticity. (*b*) Temporal evolution of the amplitude of the frontal wave in the coordinate system moving at c_{pse}. The remaining parameter is $Y_0 = 1$.

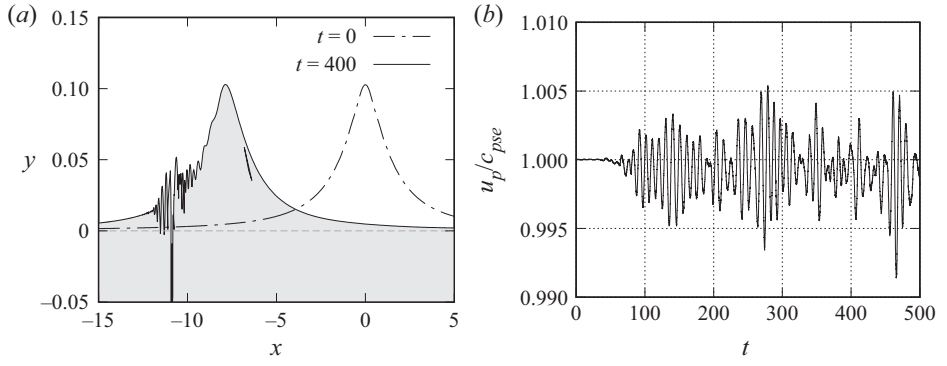

Figure 8. (*a*) Temporal evolution of the front of the nonlinear solution for $\varepsilon = 1$. The solid line corresponds to the front at $t = 400$, while the dash-dotted line corresponds to the front at $t = 0$. The fluid in the shaded area has a higher potential vorticity. (*b*) Temporal evolution of the ratio of the propagation velocity of the point vortex, u_p, to the propagation velocity obtained from the nonlinear solution, c_{pse}. The parameters used in the numerical experiment are the same as those in figure 7.

wavenumber as a function of the moving coordinate, $\zeta = x - c_{pse}t$. Figure 9(*b*) shows that the wavenumbers calculated by (5.3) agree well with those estimated from the experiment. The theoretical group velocity based on the wavenumber in the moving coordinate system, $c_{gf} = u_2 - c_{pse} + c_g$, where c_g is given by (3.9), is shown in figure 9(*c*). The group velocity in the ξ-direction is negative and vanishes at the stagnation point. Therefore, according to the experimental result shown in figure 7, the wave energy converges at the stagnation point.

5.2. *Generation of a heton-like vortex pair and the classification of the motion based on* ε

We show the results of experiments in which the parameter ε was varied, and we reveal the typical temporal evolution patterns of this system. In all the experiments in this subsection, the initial position of the point vortex was fixed at (0, 1), and there was initially no frontal displacement.

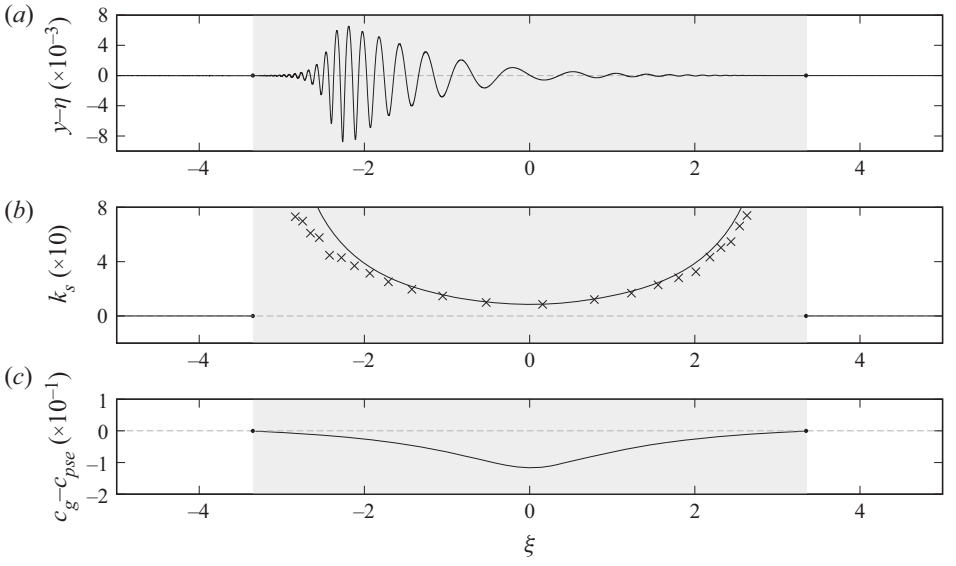

Figure 9. (*a*) The frontal disturbance caused by the difference between the η obtained from the numerical experiment at $t = 50$ and that obtained from the nonlinear pseudoimage solution. (*b*) The distribution of the stationary wavenumber. The solid line indicates the stationary local wavenumber obtained from the phase velocity of the linear frontal wave, while the crosses indicate the local wavenumber estimated from (*a*). (*c*) The group velocity of the stationary wavenumber as a function of ε. In all panels, the closed circles on the zero vertical coordinate denote the ξ coordinate of the saddle-node points, and the shaded area corresponds to the region where $u_2 - c_{pse} < 0$. The parameters used in the numerical experiment are the same as those in figure 7.

5.2.1. *An anticyclonic point vortex*

We first consider the case of an anticyclonic point vortex, i.e. $\mathrm{sgn}(\Gamma) = -1$. Figure 10 shows the temporal evolution of the potential vorticity front interacting with the point vortex with $\varepsilon = 0.1$. The temporal evolution of the velocity of the point vortex, (u_p, v_p), is shown in figure 11. The point vortex moves steadily along the topography, combining with the vortex caused by the small frontal displacement. We refer to the behaviour in which the point vortex moves along the topography as pseudoimage-type behaviour. Because the amplitude is small in this case, the disturbance retains the shape of the pseudoimage solution. When ε is larger, e.g. $\varepsilon = 1$, the disturbances collapse, similar to those shown in figure 8(*b*); however, they are classified as pseudoimages if they move along the topography.

Figure 12 shows the evolution of the front and the point vortex for $\varepsilon = 10$. The temporal evolution of (u_p, v_p) is shown in figure 13. The point vortex attracts the high potential vorticity fluid from the shallow side, forming a dipole structure. Due to the formation of this dipole structure, the point vortex has a velocity component perpendicular to the topography, v_p (see figure 13). Since the dipole structure includes both the upper-layer point vortex and the lower-layer vortex created by the potential vorticity patch, we hereafter refer to this behaviour as heton-type behaviour (Hogg & Stommel 1985).

McDonald (1998) used a 1.5-layer model to describe the existence of motion types other than those described above when the point vortex is intense, i.e. $\varepsilon \gg 1$. Figures 14 and 15 show the temporal evolution for $\varepsilon = 100$. During the early stages of the temporal evolution, the point vortex draws a large amount of fluid from the shallower side and wraps the fluid around itself. However, as more time passes, the filament wrapped around the point vortex has a weaker effect on the point vortex, and the system resembles a system with a moderate

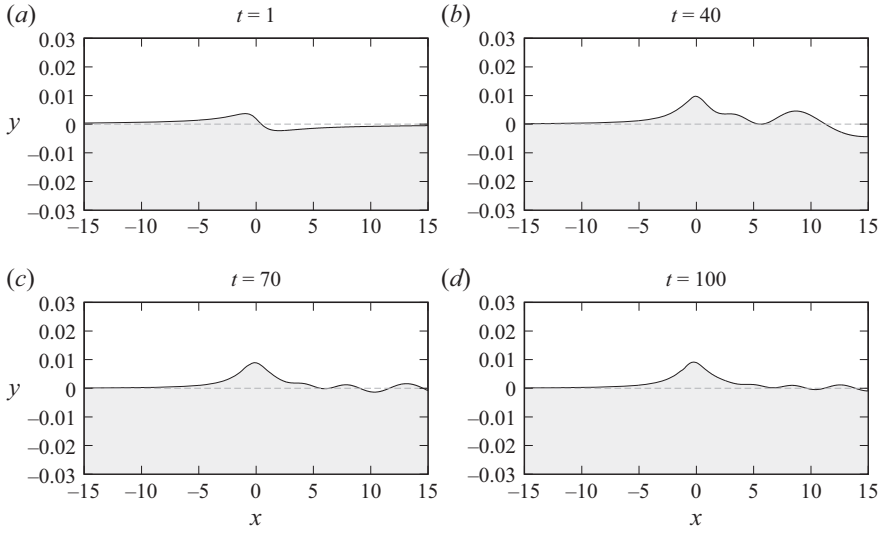

Figure 10. The temporal evolution of the potential vorticity front interacting with the anticyclonic point vortex. The parameter values are $\varepsilon = 0.1$ and $Y_0 = 1$.

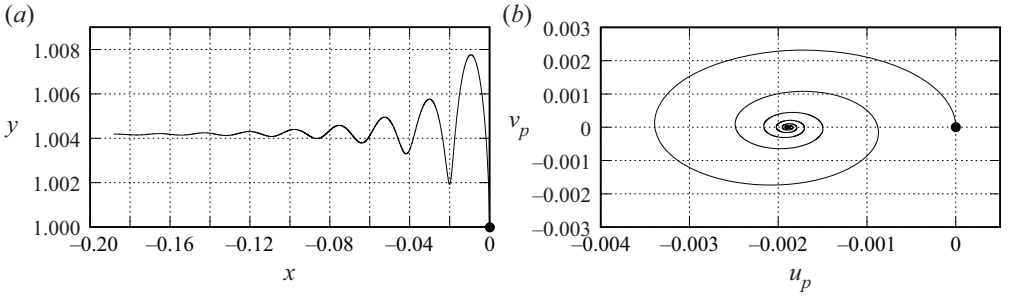

Figure 11. The trajectory of the point vortex in (*a*) x–y space and (*b*) u_p–v_p space for the case shown in figure 10, obtained by computing from $t = 0$ to $t = 100$. The starting points at $t = 0$, which are located at (0, 1) on the left and (0, 0) on the right, are indicated by the closed circles.

ε, forming a hetonic structure consisting of the filament-wrapped point vortex and the high potential vorticity patch from the shallower side.

5.2.2. *A cyclonic point vortex*

We next consider a cyclonic point vortex, i.e. $\mathrm{sgn}(\Gamma) = 1$. Figures 16 and 17 show the temporal evolution of the front and the point vortex, as well as the evolution of the velocity, (u_p, v_p), for $\varepsilon = 1$. The point vortex moves in the same direction as the topographic waves, and the small-scale wave train behind the peak of the front is confirmed. As discussed in § 3.4, this wave train occurs only for cyclonic point vortices, and it is excited by the singularity in (3.13) and (3.14) in linear theory, which was shown mathematically in Dunn *et al.* (2001). Although wave radiation was expected to weaken the isolated structure, it propagated similarly to the anticyclonic vortex, at least in our computation time. Therefore, we refer to this behaviour as pseudoimage-type behaviour. The point vortex did not drift towards the topography, as discussed by Dunn *et al.* (2001). However, the behaviour for longer computation times remains unknown.

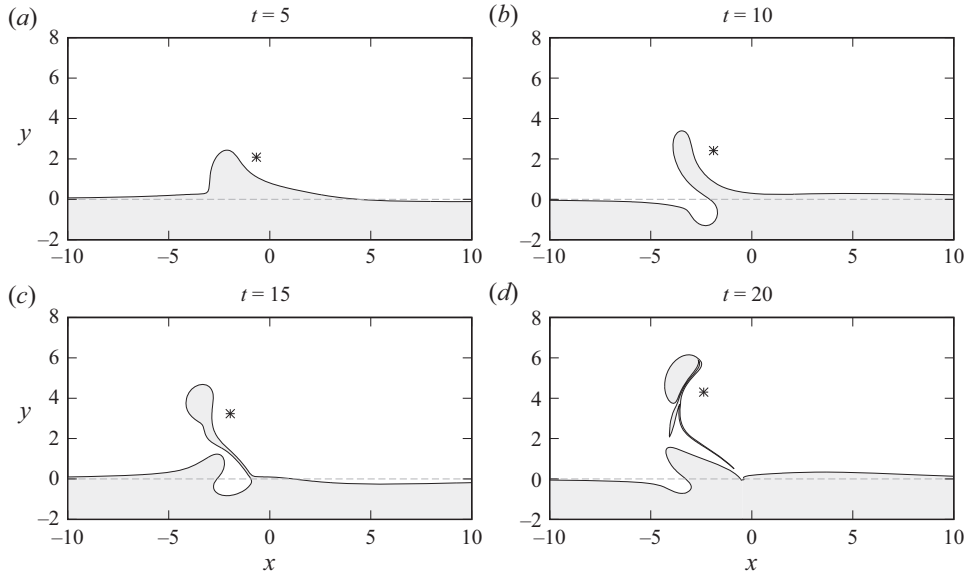

Figure 12. The temporal evolution of the potential vorticity front and the anticyclonic point vortex. The parameter values are $\varepsilon = 10$ and $Y_0 = 1$.

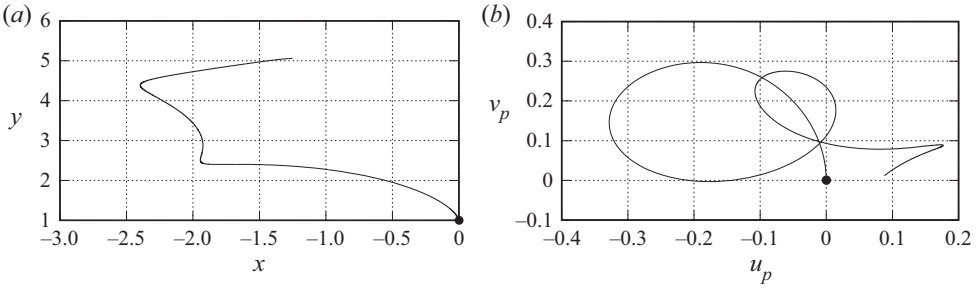

Figure 13. The trajectory of the point vortex in (*a*) x–y space and (*b*) u_p–v_p space for the case shown in figure 12, obtained by computing from $t = 0$ to $t = 30$. The starting points at $t = 0$ are indicated by the closed circles.

Figures 18 and 19 show the results for $\varepsilon = 10$. With this parameter value, the point vortex moves towards the topography in the deeper region, attracting low potential vorticity fluid. As a result, the point vortex approaches and then passes the topography, forming a dipole structure with the low potential vorticity fluid. After the dipole structure is formed, the vortices move away from the topography. We classify this behaviour as heton-type behaviour. The behaviour for $\varepsilon = 100$ is shown in figures 20 and 21. Similar to the anticyclonic case, the cyclonic point vortex initially wraps the filament around itself; however, as more time passes, the filament stops wrapping, and the vortex couples with the low potential vorticity patch in the deeper region, resulting in a heton-type motion.

5.3. *Classification of the motion based on ε and Y_0*

In the previous subsection, we used numerical experiments with the strength of the point vortex, ε, as a parameter to demonstrate that there are two types of motions that commonly

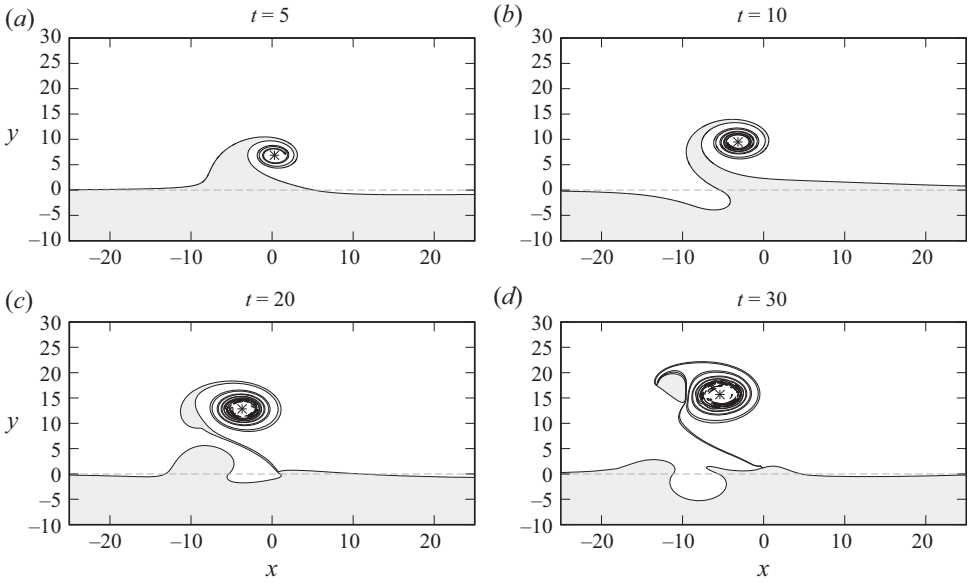

Figure 14. The temporal evolution of the potential vorticity front and the anticyclonic point vortex. The parameter values are $\varepsilon = 100$ and $Y_0 = 1$.

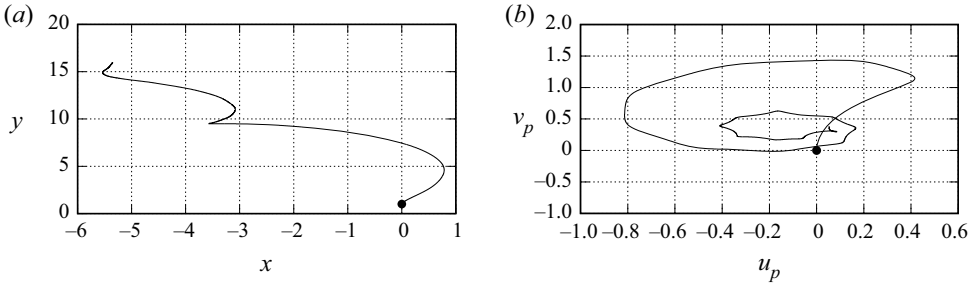

Figure 15. The trajectory of the point vortex in (*a*) x–y space and (*b*) u_p–v_p space for the case shown in figure 14, obtained by computing from $t = 0$ to $t = 30$. The starting points at $t = 0$ are indicated by the closed circles.

occur in our model. Previous studies have observed the formation of dipole structures in various systems and have identified the regions where the dipole structures form in parameter space (e.g. Shimada & Kubokawa 1997; Vandermeirsch, Carton & Morel 2003; Capet & Carton 2004). In this subsection, we conduct numerical experiments with ε and the initial location of the point vortex, Y_0, as parameters and classify the motion types in ε–Y_0 space. Based on the trajectory in u_p–v_p space, we classified pseudoimage-type motions as those where the temporal evolution of v_p asymptotically approached zero or oscillated near zero after a sufficiently long calculation, while other motions were classified as hetonic. The numerical experiments were conducted until $t = 100$. In the case that $f = 10^{-4}\,\mathrm{s}^{-1}$, $H_2 = 2000$ and $\Delta H = 1000\,\mathrm{m}$, $T = f^{-1}(\Delta H/H_2)^{-1} = 2 \times 10^4\,\mathrm{s}$, so that $t = 100$ corresponds to approximately 200 days.

Figure 22(*a*) depicts the phase diagram for the anticyclonic case, showing the distribution of the typical motion types in ε–Y_0 space. The ε–Y_0 relation at the boundary between the two motion types can be divided into two regions. For $Y_0 < 1$, the value of Y_0

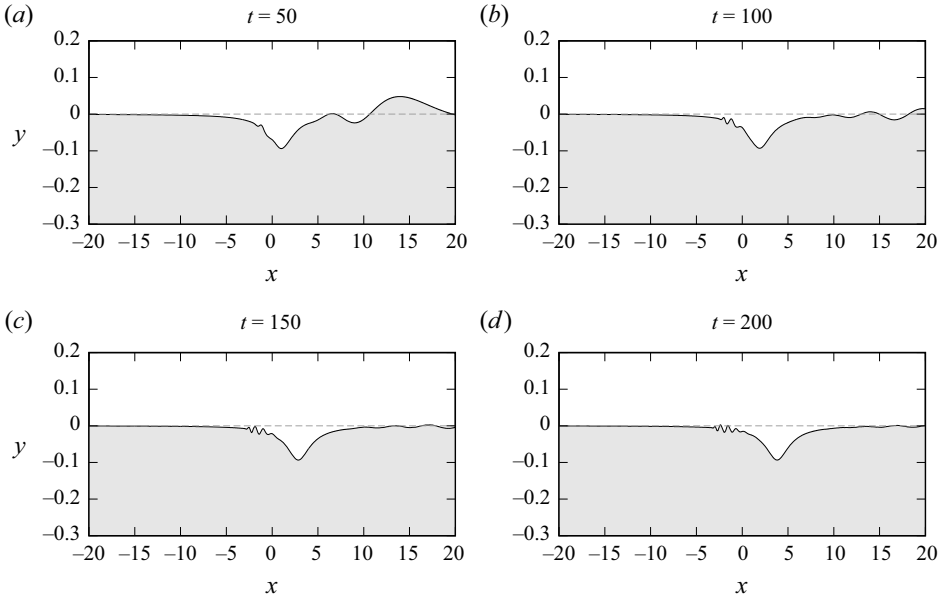

Figure 16. The temporal evolution of the potential vorticity front for a cyclonic point vortex. The parameter values are $\varepsilon = 1$ and $Y_0 = 1$.

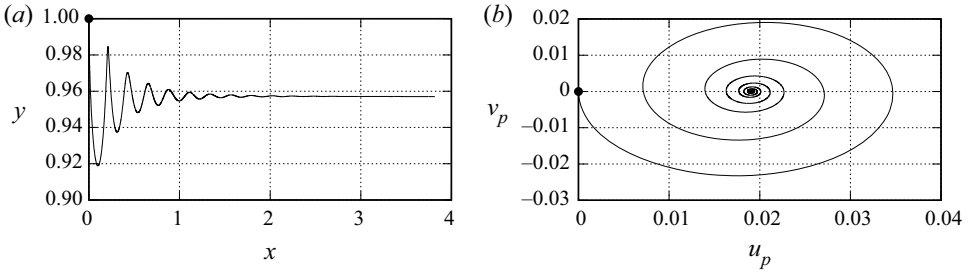

Figure 17. The trajectory of the cyclonic point vortex in (*a*) x–y space and (*b*) u_p–v_p space for the case shown in figure 16, obtained by computing from $t = 0$ to $t = 200$. The starting points at $t = 0$ are indicated by the closed circles.

changes rapidly and approaches zero at small but finite ε. This feature occurs because the point vortex and the topography are in different layers. When $Y_0 = 0$, a point vortex with negative Γ moves towards the deeper side ($Y > 0$), and if ε is small, the pseudoimage propagates along the topography with $Y \neq 0$. For $Y_0 > 1$, the slope of the boundary between the two motion types in ε–Y_0 space becomes gentler, and the slope becomes linear for sufficiently large Y_0. This feature occurs because when the value of Y_0 is initially large, the point vortex and the front interact primarily through the barotropic mode. Since the non-dimensional internal Rossby deformation radius, $\lambda_+^{-1/2}$, is approximately 0.7 in this model, the barotropic mode dominates the interaction when $Y_0 > \lambda_+^{-1/2}$. Because the frontal self-advection component has a baroclinic component even when Y_0 is large, the results of our model do not exactly match those of a barotropic model.

Figure 22(*b*) shows the phase diagram for the cyclonic case. When $Y_0 = 0$, the motion is symmetric about the x-axis, similar to the case of the anticyclonic point vortex, since

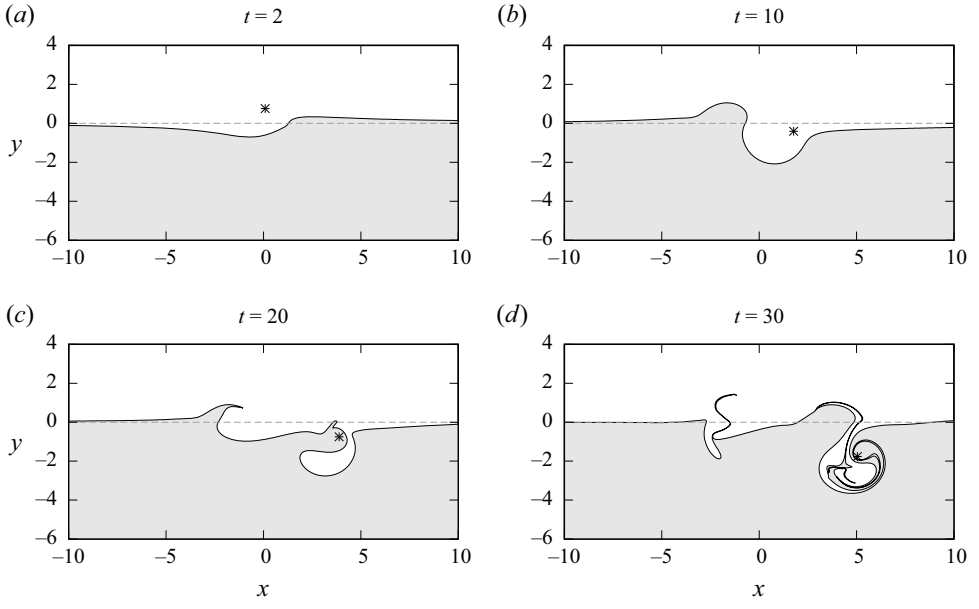

Figure 18. The temporal evolution of the potential vorticity front and the cyclonic point vortex. The parameter values are $\varepsilon = 10$ and $Y_0 = 1$.

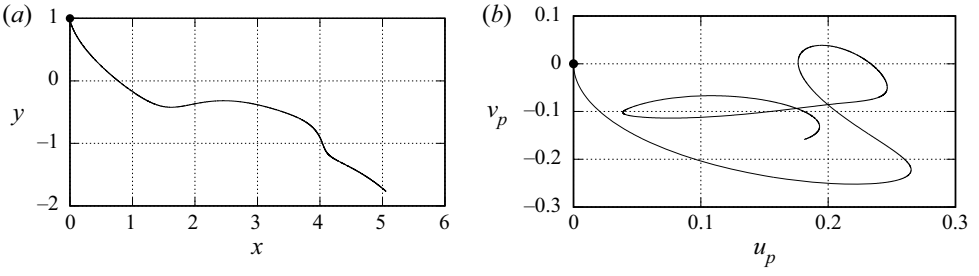

Figure 19. The trajectory of the cyclonic point vortex in (*a*) *x*–*y* space and (*b*) u_p–v_p space for the case shown in figure 18, obtained by computing from $t = 0$ to $t = 30$. The starting points at $t = 0$ are indicated by the closed circles.

$\psi_j(x, y) = -\psi_j(x, -y)$. Therefore, in the pseudoimage motion starting from $Y_0 = 0$ with $\varepsilon = 1$ shown in figure 22(*b*), the cyclonic point vortex moves to the shallower side of $y < 0$ and propagates in the opposite direction to the topographic wave, in contrast to the behaviour shown in figures 16 and 17. Although the border that divides the behaviour is unclear, all of the pseudoimages with $Y_0 > 0.25$ in our experiments have a similar structure to that shown in figure 16. The boundary between pseudoimage-type and heton-type motions is almost the same as that in the anticyclonic case. However, in the cyclonic case, the slope of this boundary is smaller than that in the anticyclonic case for $Y_0 < 1$. This difference occurs due to the difference in the direction of the displacement of the front. In the cyclonic case, as ε increases, the front tends to move away from the point vortex in the y direction, whereas in the anticyclonic case, the front approaches the point vortex as ε increases. This result indicates that for the same value of Y_0, the anticyclonic vortex is more likely to interact with the topography than the cyclonic vortex.

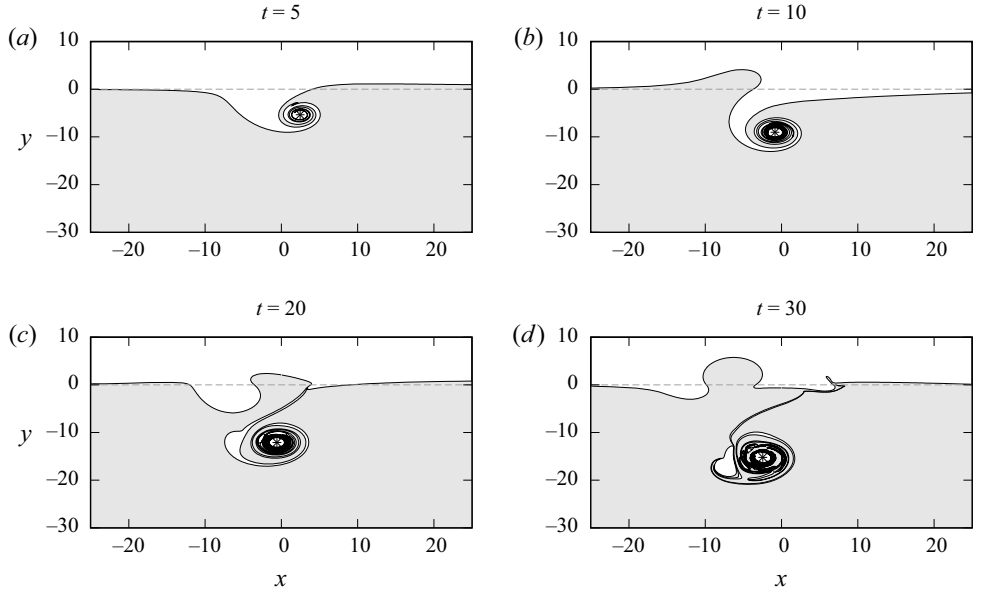

Figure 20. The temporal evolution of the potential vorticity front and the cyclonic point vortex. The parameter values are $\varepsilon = 100$ and $Y_0 = 1$.

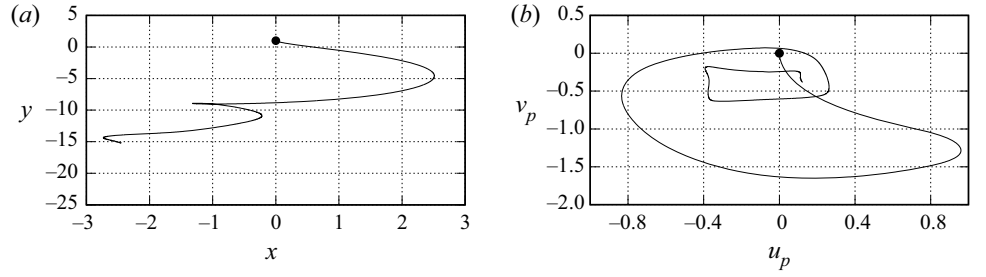

Figure 21. The trajectory of the cyclonic point vortex in (*a*) x–y space and (*b*) u_p–v_p space for the case shown in figure 20, obtained by computing from $t = 0$ to $t = 30$. The starting points at $t = 0$ are indicated by the closed circles.

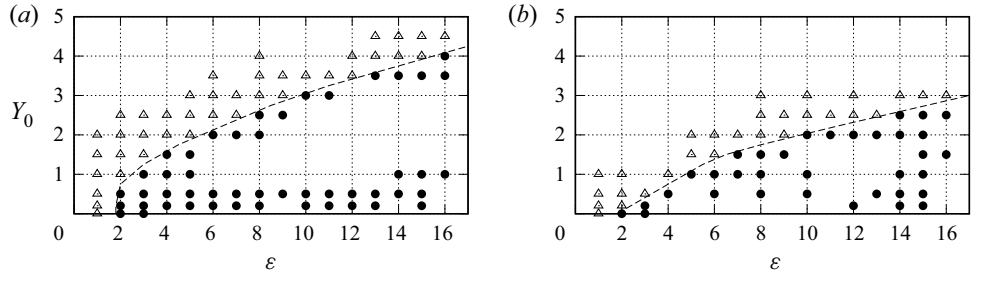

Figure 22. The diagram of the motion classification in ε–Y_0 space. The circulation of the point vortex is (*a*) $\mathrm{sgn}(\Gamma) = -1$ and (*b*) $\mathrm{sgn}(\Gamma) = 1$. The triangles and circles in the diagram indicate pseudoimage-type and heton-type motions, respectively.

6. Summary

In this study, the interaction between a point vortex in the upper layer and the step-like topography in the lower layer was investigated using a two-layer quasi-geostrophic model in the f-plane. The results can be summarized as follows.

(i) We derived the linear pseudoimage solution that steadily propagates along the topography in the two-layer system and discussed the properties of the solution. The results suggested that the steadiness of the finite-amplitude solution is lost when the solution propagates in the same direction as the topographic waves, and that the point vortex can move along the topography even when the point vortex and topography are close because they are in different layers.

(ii) The finite-amplitude, steadily propagating nonlinear pseudoimage solution was calculated numerically. We found that the flow field of the system, which includes the solution, always has saddle-node points on the potential vorticity front in a coordinate system that moves with the solution. In the numerical experiments where the nonlinear solution was used as the initial condition, short frontal waves appeared near the saddle-node point, and the symmetric structure of the front collapsed. Even after the collapse, the point vortex moved in the same manner as in the steadily propagating solutions.

(iii) We showed that the point vortex has two types of motion in this system: motion along the topography due to the pseudoimage when the strength of the point vortex, ε, is small, and motion away from the topography due to the formation of a heton-like structure when ε is large. In addition to ε, we treated the initial distance between the point vortex and the topography, Y_0, as a parameter and classified the motion types in ε–Y_0 space. We found that pseudoimage-type motion exists in the region where Y_0 is large or ε is small, while heton-type motion exists in the region where Y_0 is small or ε is large. The boundary in parameter space that separates these motions behaves differently in relation to Y_0 and the internal deformation radius. When the diagrams of the anticyclonic and cyclonic point vortices are compared, it can be seen that the anticyclonic vortex is more likely to move away from the topography than the cyclonic vortex for the same value of Y_0.

In this study, the eddy interacting with the bottom topography was approximated by a point vortex. In this approximation, the deformation and dissipation effects of the vortex itself were ignored. However, we believe that our results capture the fundamental processes in the interaction between upper eddies and the steep bottom topography because a study that used a finite-size vortex and a 1.5-layer model (Dunn 2002; Dunn *et al.* 2002) obtained similar results to a study that used a point vortex model (Dunn *et al.* 2001).

In a more realistic scenario, ε and Y_0 may vary over time. In particular, mesoscale eddies in western boundary regions continue to approach the bottom topography while interacting with the topography due to the β-effect. This suggests that the motion of a vortex can switch from along the topography to away from the topography. The change in the behaviour of the eddy over time corresponds to a transition in the type of motion in the parameter space considered in this study. Therefore, it is important to investigate this transition process to understand interactions in the western regions of the ocean. The findings of this study are the first step towards understanding this transition. The details of these transitions, especially the conditions for the formation of the vortex pair, will be investigated in future work.

Acknowledgements. The authors thank Professor K. Shimada for providing us the original contour surgery code. The authors also thank the three referees for their helpful comments on this paper.

Funding. This work was supported by JST SPRING, Grant Number JPMJSP2119.

Declaration of interests. The authors report no conflict of interest.

Author ORCIDs.
Takaaki Takeuchi https://orcid.org/0000-0002-0430-4699.

References

Azis Ismail, M.F. & Ribbe, J. 2019 On the cross-shelf exchange driven by frontal eddies along a western boundary current during austral winter 2007. *Estuar. Coast. Shelf Sci.* **277**, 106314.

Baird, M.E. & Ridgway, K.R. 2012 The southward transport of sub-mesoscale lenses of bass strait water in the centre of anti-cyclonic mesoscale eddies. *Geophys. Res. Lett.* **39**, L02603.

Baker-Yeboah, S., Flierl, G.R., Sutyrin, G.G. & Zhang, Y. 2010 Transformation of an Agulhas eddy near the continental slope. *Ocean Sci.* **6**, 143–159.

Bell, G.I. 1989 Interaction between vortices and waves in a simple model of geophysical flow. *Phys. Fluids* A **2**, 575–586.

Bell, G.I. & Pratt, L.J. 1992 The interaction of an eddy with and unstable jet. *J. Phys. Oceanogr.* **22**, 1229–1244.

Capet, X.J. & Carton, X.J. 2004 Nonlinear regimes of baroclinic boundary currents. *J. Phys. Oceanogr.* **34**, 1400–1409.

Carton, X., Daniault, N., Alves, J., Cherubin, L. & Ambar, I. 2010 Meddy dynamics and interaction with neighboring eddies southwest of Portugal: observations and modeling. *J. Geophys. Res.* **115**, C06017.

Chelton, D.B., Schlax, M.G. & Samelson, R.M. 2011 Global observations of nonlinear mesoscale eddies. *Prog. Oceanogr.* **92**, 167–216.

Dong, C., McWilliams, J.C., Liu, Y. & Chen, D. 2014 Global heat and salt transports by eddy movement. *Nat. Commun.* **5**, 3294.

Dritschel, D.G. 1988 Contour surgery: a topological reconnection scheme for extended integrations using contour dynamics. *Comput. Phys.* **77**, 240–266.

Dunn, D.C. 2002 The evolution of an initially circular vortex near an escarpment. Part 2. Numerical results. *Eur. J. Mech.* B*/Fluids* **21**, 677–699.

Dunn, D.C., McDonald, N.R. & Johnson, E.R. 2001 The motion of a singular vortex near an escarpment. *J. Fluid Mech.* **448**, 335–365.

Dunn, D.C., McDonald, N.R. & Johnson, E.R. 2002 The evolution of an initially circular vortex near an escarpment. Part 1. Analytical results. *Eur. J. Mech.* B*/Fluids* **21**, 657–675.

Flierl, G.R, Larichev, V.D., McWilliams, J.C. & Reznik, G.M. 1980 The dynamics of baroclinic and barotropic solitary eddies. *Dyn. Atmos. Oceans* **5**, 1–41.

Hogg, N.G. & Stommel, H.M. 1985 The heton an elementary interaction between discrete baroclinic geostrophic vortices, and its implications concerning eddy heat-flow. *Proc. R. Soc. Lond.* A **397**, 1–20.

Hughes, C.W. & Miller, P.I. 2017 Rapid water transport by long-lasting modon eddy pairs in the southern midlatitude oceans. *Geophys. Res. Lett.* **44**, 12375–12384.

Itoh, S. & Sugimoto, T. 2001 Numerical experiments on the movement of a warm-core ring with the bottom slope of a western boundary. *J. Geophys. Res.* **106**, 26851–26861.

Itoh, S. & Yasuda, I. 2010 Characteristics of mesoscale eddies in the Kuroshio–Oyashio extension region detected from the distribution of the sea surface height anomaly. *J. Phys. Oceanogr.* **40**, 1080–1034.

Kaneko, H., Itoh, S., Kouketsu, S, Okunishi, T., Hosoda, S. & Suga, T. 2015 Evolution and modulation of a poleward-propagating anticyclonic eddy along the Japan and Kuril-Kamchatka trenches. *J. Geophys. Res.* **120**, 4418–4440.

de Marez, C., Carton, X., Morvan, M. & Reinaud, J.N. 2017 The interaction of two surface vortices near a topographic slope in a stratified ocean. *Fluids* **2**, 57.

McDonald, N.R. 1998 Motion of an intense vortex near topography. *J. Fluid Mech.* **367**, 359–377.

Moreé, J.J., Garbow, B.S. & Hillstrom, K.E. 1980 User guide for MINPACK-1. *Tech. Rep.* ANL-80-74. Argonne National Laboratory.

Morel, Y. & McWilliams, J. 2001 Effects of isopycnal and diapycnal mixing on the stability of oceanic currents. *J. Phys. Oceanogr.* **31**, 2280–2296.

Rhines, P.B. 1977 The dynamics of unsteady currents. In *The Sea – Ideas and Observations of Progress in the Study of the Seas* (ed. E. D. Goldberg, I. McCave, J. O'Brien & J. Steele), vol. 6, pp. 189–318. John Wiley and Sons.

RIBBE, J., TOASPERN, L., WOLFF, J. -O. & AZIS ISMAIL, M.F. 2018 Frontal eddies along a western boundary current. *Cont. Shelf Res.* **165**, 51–59.

RICHARDSON, P.L. & TYCHENSKY, A. 1998 Meddy trajectories in the Canary Basin measured during the SEMAPHORE experiment. *J. Geophys. Res.* **103**, 25029–25045.

SCHAEFFER, A., GRAMOULLE, A., ROUGHAN, M. & MANTOVANELLI, A. 2017 Characterizing frontal eddies along the East Australian Current from HF radar observations. *J. Geophys. Res.* **122**, 3964–3980.

SERRA, N. & AMBAR, I. 2002 Eddy generation in the Mediterranean undercurrent. *Deep-Sea Res. II* **49**, 4225–4243.

SERRA, N., AMBAR, I. & BOUTOV, D. 2010 Surface expression of Mediterranean water dipoles and their contribution to the shelf/slope - open ocean exchange. *Ocean Sci.* **6**, 191–209.

SHIMADA, K. & KUBOKAWA, A. 1997 Nonlinear evolution of linearly unstable barotropic boundary currents. *J. Phys. Oceanogr.* **27**, 1326–1348.

SPALL, M.A., PICKART, R.S., FRATANTONI, P.S. & PLUEDDEMANN, A.J. 2008 Western Arctic shelfbreak eddies: formation and transport. *J. Phys. Oceanogr.* **38**, 1644–1668.

STERN, M.E. 1975 Minimal properties of planetary eddies. *J. Mar. Res.* **40**, 57–74.

STERN, M.E. & FLIERL, G.R. 1987 On the interaction of a vortex with a shear flow. *J. Geophys. Res.* **92**, 10733–10744.

VANDERMEIRSCH, F.O., CARTON, X.J. & MOREL, Y.G. 2003 Interaction between an eddy and a zonal jet. Part 1. One-and-a-half-layer model. *Dyn. Atmos. Oceans* **36**, 247–270.

WANG, X. 1991 Interaction of an eddy with a continental slope. PhD thesis, Massachusetts Institute of Technology/Woods Hole Oceanographic Institution.

WHITE, A.J. & MCDONALD, N.R. 2004 The motion of a point vortex near large-amplitude topography in a two-layer fluid. *J. Phys. Oceanogr.* **34**, 2808–2824.

YASUDA, I., OKUDA, K. & HIRAI, M. 1992 Evolution of a Kurosio warm-core ring - variability of the hydrographic structure. *Deep-Sea Res.* **39**, S131–S161.

ZABUSKY, N.J., HUGHES, M. & ROBERTS, K.V. 1979 Contour dynamics for the Euler equations in two dimensions. *J. Comput.* **30**, 96–106.

ZHANG, Y., PEDLOSKY, J. & FLIERL, G.R. 2011 Shelf circulation and cross-shelf transport out of a bay driven by eddies from an open-ocean current. Part 1. Interaction between a barotropic vortex and a steplike topography. *J. Phys. Oceanogr.* **41**, 889–910.